OPEN ACCESS

Characterisation of a near-infrared (NIR) fluorescence imaging systems intended for hybrid gamma-NIR fluorescence image guided surgery

View the article online for updates and enhancements.

IOP **ebooks**™

Bringing you innovative digital publishing with leading voices to create your essential collection of books in STEM research.

Start exploring the collection - download the first chapter of every title for free.

Characterisation of a near-infrared (NIR) fluorescence imaging systems intended for hybrid gamma-NIR fluorescence image guided surgery

A.M. Almarhaby,[a,b,1] J.E. Lees,[a] S.L. Bugby,[a] M.S. Alqahtani,[c] L.K. Jambi,[d] W.R. McKnight[a] and A.C. Perkins[e,f]

[a] *Space Research Centre, Michael Atiyah Building, University of Leicester, Leicester, LE1 7RH, U.K.*

[b] *Radiology Department, King Fahd General Hospital, Postcode: 23325, Jeddah, Kingdom of Saudi Arabia*

[c] *Radiological Sciences Department, Faculty of Applied Medical Sciences, King Khalid University, Postcode: 3665, Zip code 61481, Abha, Kingdom of Saudi Arabia*

[d] *Radiological Sciences Department, Faculty of Applied Medical Sciences, King Saud University, Postcode: 10219, Zip code 11433, Riyadh, Kingdom of Saudi Arabia*

[e] *Radiological Sciences, School of Medicine, University of Nottingham, Nottingham, NG7 2UH, U.K.*

[f] *Medical Physics and Clinical Engineering, Nottingham University Hospitals NHS Trust, Nottingham, NG72UH, U.K.*

E-mail: ama78@leicester.ac.uk

ABSTRACT: A novel hand-held hybrid optical-gamma camera (HGC) has previously been described that is capable of displaying co-aligned images from both modalities in a single imaging system. Here, a dedicated NIR imaging system for NIR fluorescence surgical guidance has been developed for combination with the HGC. This work has evaluated the performance of two NIR fluorescence imaging systems using phantom studies, various fluorophores and various experimental configurations. The threshold detectable concentration of ICG and 800CW dyes were investigated for both systems. Bespoke lymph node phantoms simulating metastases and tissue-like layers were constructed to evaluate the detection capability. ICG could be detected at a minimum concentration of 1 µM for each camera. The lower thresholds for 800CW were 10^{-2} and 10^{-3} µM for the modified and NIR cameras, respectively. Both cameras were unable to detect small-sized targets within a 3 mm depth, but were able to identify larger targets as deep as 7 mm. Further improvements are required to optimise the NIR-fluorescence systems for subsequent combination with the HGC to undertake dual gamma-NIR fluorescence intraoperative imaging.

---

[1]Corresponding author.

Contents

1 Introduction

Cancer remains one of the leading causes of morbidity and mortality worldwide [1]. Surgery is the oldest form of treatment and is still currently considered the most effective method for solid tumour resection. Although modern preoperative imaging technologies have significantly improved the success of cancer surgery, there is still an unfulfilled demand for additional guidance during the surgical procedure [2, 3]. This stems from the fact that surgeons cannot precisely detect or 'see' the target tissue margins that need to be resected, whilst preserving non-diseased tissues.

Recently, a growing body of research has shown that fluorescent light within the near-infrared (NIR) window has the potential to provide the basis for a new intraoperative imaging technology for sentinel lymph node (SLN) localisation and the assessment of tumour margin delineation [4]. This new approach has a higher spatial resolution than conventional radiological and nuclear medicine technologies, providing better discrimination between diseased and healthy tissues [5]. It has been reported clinically that the NIR florescence method has a better detection ability compared to the current gold standard ^{99m}Tc probe guided techniques for SLN detection. For instance, a prospective

study comparing both methods was conducted on a group of 134 patients to resect axillary SLNs in early breast cancer. This cohort offered a total of 246 SLNs, detected by one or both techniques. The ^{99m}Tc method detected 231 SLNs (93.9%), while the NIR fluorescence detected 245 of 246 (99.6%) of the total SLNs found during surgical procedures [6]. Several other studies have indicated that NIR fluorescence imaging for detecting SLNs shows a sensitivity of 97–100% and was associated with low toxicity and few side effects, such as allergic reactions [7–9].

During the last decade, there have been an increasing number of NIR fluorescence imaging systems approved by the FDA for use in the operating theatre [3, 10]. These are not only for open surgery procedures, but also for laparoscopic, thoracoscopic, and robotic surgery. Examples of the currently available intraoperative systems are: PDE$^{®}$ manufactured by Hamamatsu [11], the SPY fluorescence imaging system by Novadaq [12], the FLARE^{TM} system from the Frangioni Laboratory [13], and Fluobeam$^{®}$ developed by Fluoptics [14]. The Artemis, a recent imaging system developed for real-time guidance during surgery, has been developed by Quest Medical Imaging (Essex UK) and the Leiden University Medical Centre in Holland [15]. This imaging system has been evaluated *in vivo* for tumours, SLNs and vital structure visualisation, demonstrating the possibility of its use in the operating room, albeit with further improvements.

Other systems for *in vivo* molecular imaging are also commercially available, providing NIR fluorescence and optical imaging for small animal studies. For example, the Pearl Impulse Small Animal Imager (LI-COR) combines two laser excitation systems in a closed box in which the sample is isolated from external sources of light [16]. This system is light-tight, offering high-quality NIR fluorescence images with very low background signal, and therefore has an exceptional imaging sensitivity, even for deep targets.

Despite the fact that the NIR fluorescence approach has emerged as a new intraoperative imaging technique, it has certain limitations with regards to the limited depth penetration to which it is capable, which is about 1–2 cm under the skin [3, 4, 10]. To overcome this impediment, gamma emitting and NIR fluorescence agents have been combined for SLN navigation. This complementary combination allows the use of the penetrative nature of radioactivity to perform gross navigation of the lesion, while the superior spatial resolution of NIR fluorescence assists surgeons in detailed target identification and resection [4]. This concurrent use of radio-fluorescence imaging has the potential to reduce surgical time, anaesthesia, costs and improve cancer treatment outcomes.

In 2011, van der Poel et al. used the ICG-^{99m}Tc-nanocolloid to detect the location of SLNs in 11 patients who underwent robot-assisted laparoscopic prostatectomy (RALP) [17]. SLNs were localised preoperatively using single-photon emission computed tomography/computed tomography (SPECT/CT) imaging. Then, fluorescence imaging enabled intraoperative identification with improved surgical guidance, particularly for SLNs at sites with high radioactive background signals. Brouwer et al. also evaluated this integral modality of ICG-^{99m}Tc tracers to detect SLNs in 11 patients with head and neck melanoma in 2012 [18]. This allowed preoperative visualisation and intraoperative guidance for SLN resection in head and neck cancer patients. Another study performed by van den Berg et al. in 2012 studied the concomitant application of ICG-^{99m}Tc for SLN mapping in oral cavity malignancies [19]. The combined use of radio-fluorescence imaging demonstrated the feasibility of SLN detection, in particular when found in close proximity to the primary site. Jeschke et al. (2012) investigated the use of a ^{99m}Tc-nanocolloid which was injected preoperatively with immediate injection of ICG before surgery for lymph node mapping in prostate

patients [20]. Two separate systems were used in this study with a laparoscopic fluorescence imaging system designed to visualise lymphatic vessels and nodes. The second system was a laparoscopic gamma probe that could detect the radio localisation in SLNs. This study showed that fluorescence navigation has the potential to be an effective tool not only for lymph nodes but also for lymphatic vessel visualisation. However, these findings were based on the sequential application of pre- and intraoperative gamma imaging/probing and real-time fluorescence imaging due to the lack of any single system that combines gamma and NIR fluorescence images during surgery.

A recent study by Kang et al. in 2018 presented a proof-of-concept for a prototype multimodal laparoscope that enables NIR/gamma/visible imaging using a wavelength division multiplexing method [21]. They evaluated each imaging method and obtained simultaneous NIR/gamma/visible fused images of Eppendorf tubes containing a mixture of ICG and ^{99m}Tc that were placed within a dark box.

A novel small field of view (SFOV) hand-held hybrid optical gamma camera (HGC) has already been developed for scintigraphic procedures and intraoperative SLN mapping [22, 23]. This camera combines gamma and optical images to provide high spatial resolution and demonstrates a new possibility for SLN identification during surgery [24]. This paper describes research undertaken to develop and integrate a new NIR fluorescence imaging system for combination with the HGC gamma imaging system. The eventual aim of this is that the penetrative nature of gamma emission, together with the high spatial resolution of fluorescence imaging, can be combined simultaneously in a single device. This work has evaluated two NIR fluorescence cameras using two different NIR florescent contrast agents at various concentrations and with different formats and phantoms, with the ultimate focus on detection ability in order to identify areas for future development.

2 Materials and methods

Different experimental configurations were used to study system performance under a range of simulated situations with variables including dye concentration, depth of target and target diameter. All images were acquired with the room lights turned off to reduce possible interference from visible light. A primary aim was to measure the signal-to-noise ratio (SNR), which indicates a system's ability to detect a particular feature in an image. The other quantity investigated was the contrast-to-noise ratio (CNR), which is a measure of how easily different regions can be distinguished from each other. Each of these quantities can be calculated using equations (2.1) and (2.2).

$$SNR = \frac{Mean}{\sigma_{Background}} \qquad (2.1)$$

$$CNR = \frac{Mean\text{-}Mean_{Background}}{\sigma_{Background}} \qquad (2.2)$$

2.1 NIR fluorescence imaging cameras

Two cameras were used in this experiment to detect the fluorescence agents: the USB 2 uEye XS industrial camera, and the USB 3 uEye UI-3240CP Rev. 2 camera [25, 26], these are described in more detail in the following sections.

2.1.1 The XS camera

The USB 2 uEye XS optical camera consisted of a lens, autofocus system and a 5 megapixel CMOS sensor with a pixel size of $1.4\,\mu m$ [25]. The sensor provided a resolution of 2592×1944 pixels with a frame rate of 15 fps. This lightweight camera, with a mass of 20 g, has dimensions of $26.5\,mm \times 23.0\,mm \times 21.5\,mm$. Camera readout was via a USB 2.0 interface and operation is controlled using Imaging Development Systems' (IDS) software suite to enable image acquisition. This optical camera has already been incorporated with the HGC system to obtain images in the visible wavelengths; it was not designed for NIR fluorescence imaging and therefore its infrared-blocking filter was removed for modification to act as a NIR fluorescence camera.

2.1.2 The CP camera

The UI-3240 CP camera contained one of the most light-sensitive sensors in the IDS product portfolio, a 1.3 megapixel CMOS sensor with a $5.3\,\mu m$ pixel size [26]. It had a resolution of 1280×1024 pixels at a frame rate of 60 fps. The dimensions of this camera were $29.0\,mm \times 29.0\,mm \times 29.0\,mm$ with a weight of 52 g. This NIR camera was connected to a manual focussing lens that had a focal length of 6 mm. It was directly connected to a computer via USB 3.0 interface that ran using its own software program.

2.2 NIR fluorescence probes

The most commonly used NIR fluorescence contrast agent in the 800–900 nm range is indocyanine green (ICG) [6, 10, 27]. It has been approved for several medical applications by the Food and Drug Administration (FDA) and the European Medicines Agency (EMA) [6]. When ICG is injected into the patient, it binds with serum albumin, the most abundant protein in blood, and emits light between 800 to 840 nm after excitation. ICG has been used for lymph node mapping in various types of tumour including breast cancer, melanoma, anal cancer, colorectal neoplasia, gynaecological cancers and head and neck lesions [3, 27].

More recently, an emerging NIR fluorescence dye with the product name IRDye® 800CW has been introduced for molecular imaging. It has an excitation peak at 770 nm and a light emission peak at 805 nm [3]. This new agent has been evaluated in animal models and is currently being used in phase II clinical trials, both in Europe and in the U.S. It has been reported that, *in vivo*, the IRDye® 800CW has lower toxicity than ICG and conjugates with biomolecules in a straightforward manner [28–30]. Figure 1 shows the excitation and emission spectrum properties of ICG and IRDye® 800CW contrast agents.

Both cameras were evaluated using various concentrations of both ICG and IRDye® 800CW. ICG was dissolved in deionised water and serial dilutions made to obtain concentrations ranging from 1 mM to 100 fM. IRDye® 800CW was dissolved in phosphate-buffered saline (PBS) and different concentrations were obtained in the same manner ranging from $1\,\mu M$ to 100 fM. For each concentration, a volume of $100\,\mu L$ was added to a 96-well plate, and individual wells were imaged with each camera in different experimental setups. ImageJ software was used to measure the mean signal of the regions of interest (ROIs), whilst background signals were measured outside the ROIs [31]. The camera noise was considered to be the standard deviation within the background area
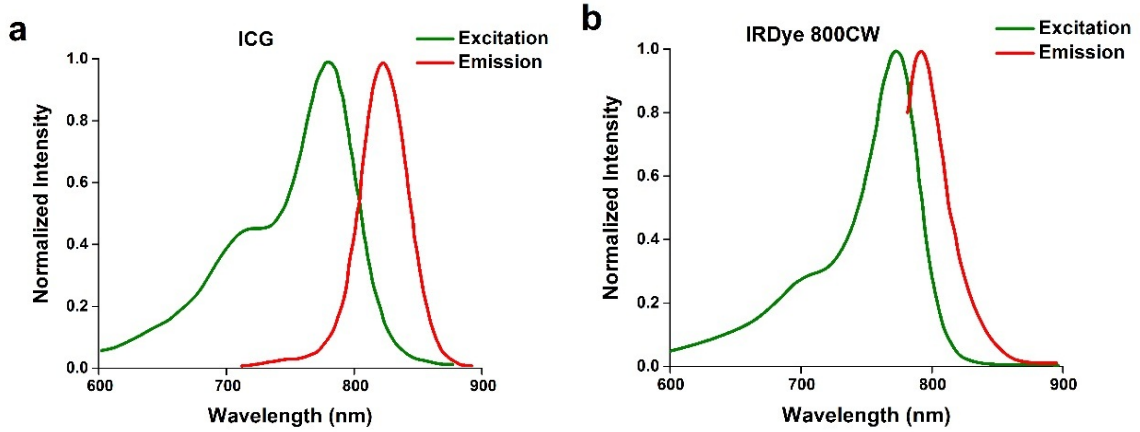
Figure 1. The excitation and emission spectra of the fluorescent dyes (a) ICG and (b) IRDye®800CW [3, 29].

($\sigma_{Background}$). SNRs were calculated using equation (2.1), and the resultant curves were compared to the data published for the Pearl and Artemis devices [15].

2.3 Excitation light

A NIR LED ring with a peak intensity at 740 nm was used as the illumination source [32]. The full-width at half maximum (FWHM) of the spectral intensity is 30 nm, which makes this product suitably matched to the excitation wavelength of both fluorescence dyes. This geometry is a ring with a diameter of 70.8 mm and height of 70.8 mm and of 17 mm, respectively. It provides a radiant flux of 80 W/m^2 and spot size with a 100 mm diameter when placed at a distance of 40 mm from the targeted surface.

2.4 Filters

Two NIR optical bandpass filters were used to select narrowband emission wavelengths from the target with the aim of rejecting the excitation light and enhancing the detectability of the emitted light. Multi-layer hard-coating bandpass filters centred at 850 nm with a FWHM of 100 nm were fitted in each camera during the study [33]. For the XS camera, a square filter with dimensions of 8 mm^2 and a thickness of 1.1 mm was fixed in front of the lens; a circular bandpass filter, with an 18 mm diameter and a 1.1 mm thickness and the same transmission properties, was placed between the manual lens and the sensor of the CP camera.

2.5 Phantoms

To evaluate the SLN mapping and target navigation capabilities of the imaging system, three phantoms were constructed in-house; two were made of polymethyl methacrylate (PMMA), also known as acrylic glass, to simulate lymph nodes. For the tissue-like phantom, a mixture of different components was used to build a phantom with optical properties similar to that of human tissues. These phantoms are described in more detail in the following sections.

2.5.1 Lymph node phantoms

The first phantom was a plastic slab with dimensions of 80 mm×80 mm, 8 mm thick. It was designed with a 10 mm dimeter well, 6 mm deep, positioned centrally in the phantom. This phantom was used to simulate a large lesion (LL) in the body. The second phantom had a rectangular shape with dimensions of 26 mm × 14.5 mm and a thickness of 7 mm. It consisted of four columns, each having five different-sized holes with a fixed depth of 5 mm and diameters of 4, 3, 2, 1 and 0.5 mm. These different diameter sizes were used to simulate metastatic lesions (ML). Figure 2 is a schematic diagram illustrating each of these designs.
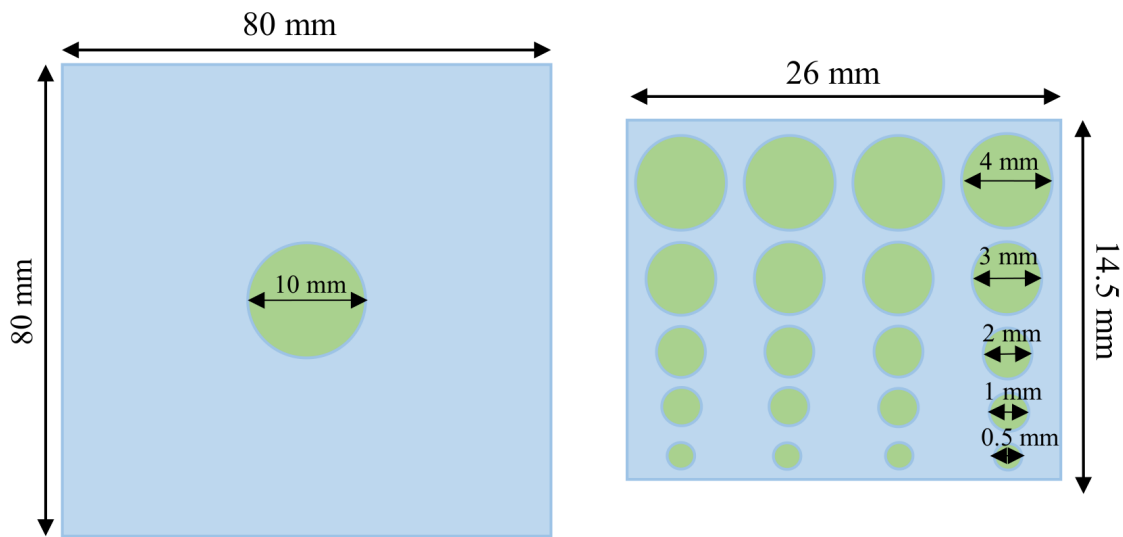

Figure 2. Illustration of the lymph node phantoms representing a large lesion (LL) on the left and metastatic lesions (ML) on the right.

2.5.2 The optical tissue-like phantom

In order to characterise a target at depth within the body, a phantom with tissue-like optical properties was created based on a previously published study [34]. The phantom was made of a transparent silicone rubber in which scattering materials were mixed [35]. The scattering materials were Al_2O_3 and a cosmetic powder, which were used to imitate scattering substances under the human skin such as water, lipids, oxyhemoglobin, deoxyhemoglobin, melanin and fat [36–38]. The phantom components were well-mixed in a glass beaker using a mixture of 97.52% silicone rubber, 2.22% Al_2O_3 and 0.26% cosmetic powder [39]. Then, the mixture was moulded in a standard Petri dish using different volumes to build phantoms with different centroid thicknesses of between 1 to 4 mm. The mixture was then kept for more than 48 hrs. at room temperature to ensure it was completely cured. After that, it was extracted from the Petri dishes with the final shapes shown in figure 3.
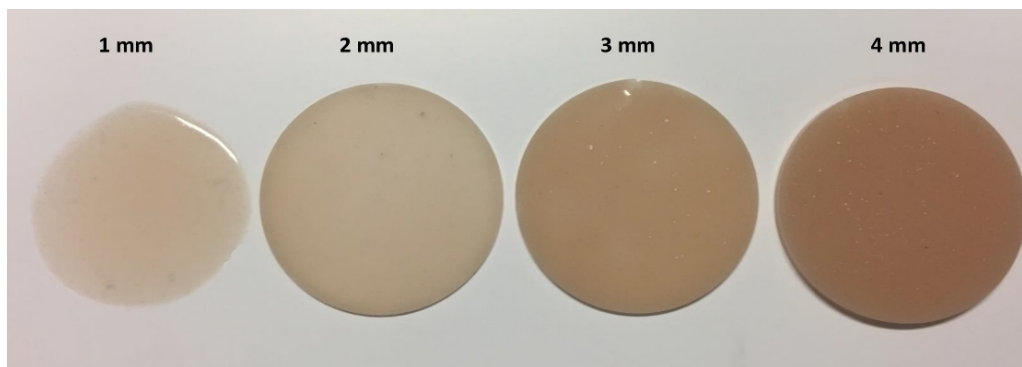
Figure 3. An image of the final constructed tissue phantoms with different thicknesses ranging from 1 mm to 4 mm.

2.6 NIR fluorescence imaging procedures

In this experiment, two identical setups were used for both the XS and CP cameras, where the excitation light was placed in two positions, namely above and to the side of the phantoms, as depicted in figure 4. In the parallel position, each of the cameras was fixed in the middle of the excitation ring.
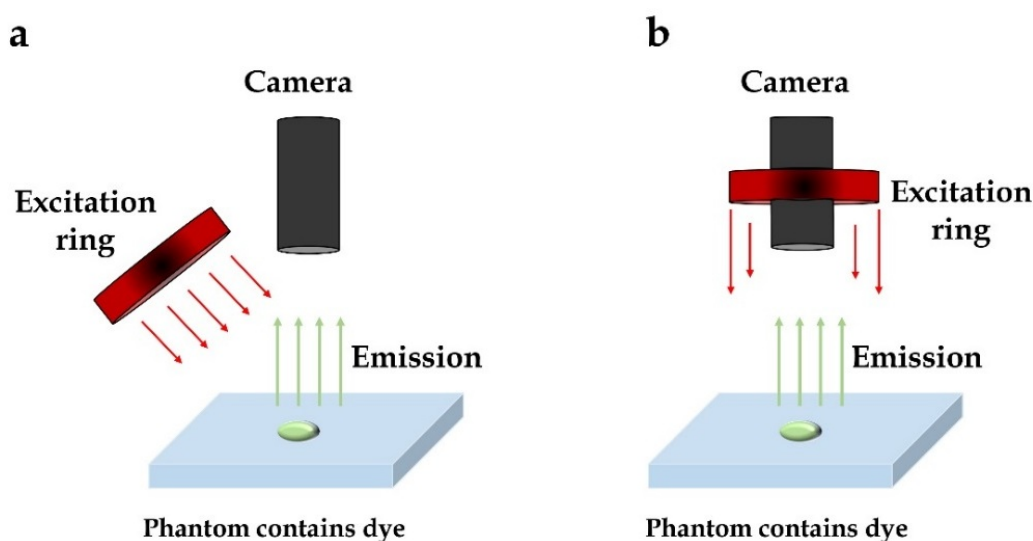

Figure 4. The experimental setup using the excitation ring to the side (a) and parallel (b) to the imaging field.

3 Results

3.1 Concentration-based sensitivity analysis

Images of the 96-well plate were acquired for concentration series of both NIR fluorophores described above to estimate the concentration-dependent sensitivity of each camera. The resultant SNR curves were plotted as a function of concentration and compared to the Pearl and Artemis imaging systems from a study conducted by van Driel et al. in 2015 [15].

For the ICG dye, figure 5(a) shows that the SNR of the Pearl increased with increasing concentration and peaked at a concentration of approximately $10\,\mu$M. After this peak, the SNR started to decrease due to peak quenching. The Artemis registered its lowest reliable concentration of $10^{-2}\,\mu$M, and its SNR peaked earlier than the Pearl due to sensor saturation [15]. The CP and XS cameras were unable to distinguish lower concentrations due to high background noise from the bright reflection of the LED ring which was visible as a circular spot on the plastic well-plate. Also, it can be seen that the CP camera registered higher SNR at lower concentration compared to the other systems. Both the XS and CP were found to have a threshold for reliable ICG detection of $1\,\mu$M and reached maximum SNRs at concentrations of about $10\,\mu$M using the ICG.

Similarly, the 96-well plate was imaged for a serial dilution of 800CW dye and compared to the Pearl and Artemis, as illustrated in figure 5(b). The SNR curve for the Pearl began from almost zero followed by a considerable increase at a concentration of $10^{-3}\,\mu$M, which then increased as the concentrations of 800CW increased, demonstrating its higher sensitivity for detecting very low concentrations [15]. The SNR started to increase for the CP, indicating its minimum detectable concentration at $10^{-3}\,\mu$M, and then reached its peak earlier than all the cameras at about $10^{-3}\,\mu$M. The lowest reliably detectable concentration for the XS was $10^{-2}\,\mu$M, which recorded a maximum SNR at approximately $1\,\mu$M but at lower values compared to the other three cameras.
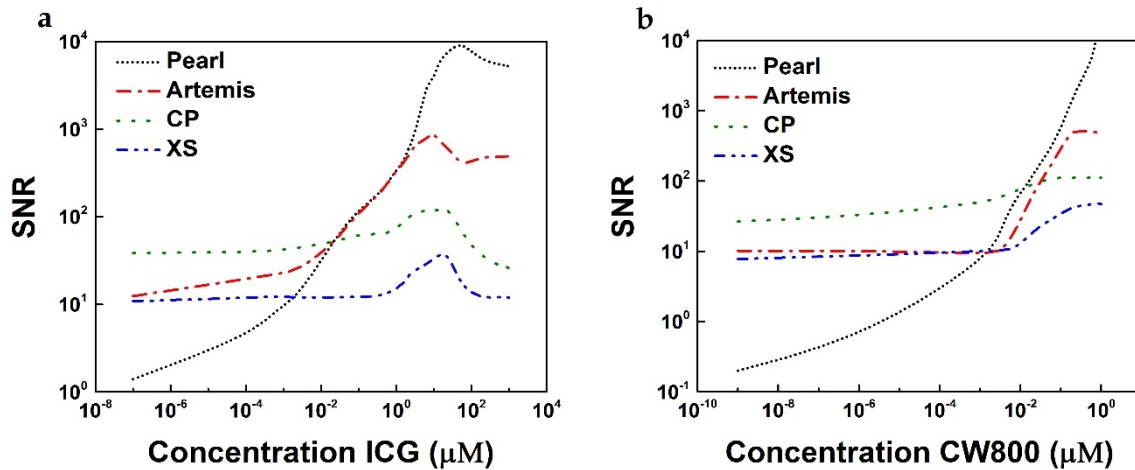

Figure 5. Signal-to-noise ratio (SNR) for series dilutions of ICG (a) and 800CW (b) imaged in 96-well plate for CP and XS cameras, as compared to the Pearl and Artemis.

3.2 CNR as a function of target diameter

The ML phantom was used to investigate the detection ability of each camera for imaging simulated small-sized metastatic lesions which contain various concentrations with focal spots between 4 and $0.5\,$mm in diameter. Each column was filled with different concentrations of ICG (15, 10, 5 and $2.5\,\mu$M) from left-to-right. For 800CW, the phantom was also filled with concentrations of 1, 0.2, 0.05 and $0.013\,\mu$M from left-to-right. At a $10\,$cm distance, one column containing optimal concentrations resulting from a dilution series in concentration-based sensitivity analysis was chosen for each dye. These optimal concentrations were 10 and $0.2\,\mu$M for ICG and 800CW, respectively. Figure 6 shows the images that were obtained for the MLs phantom using the CP and XS with both dyes.

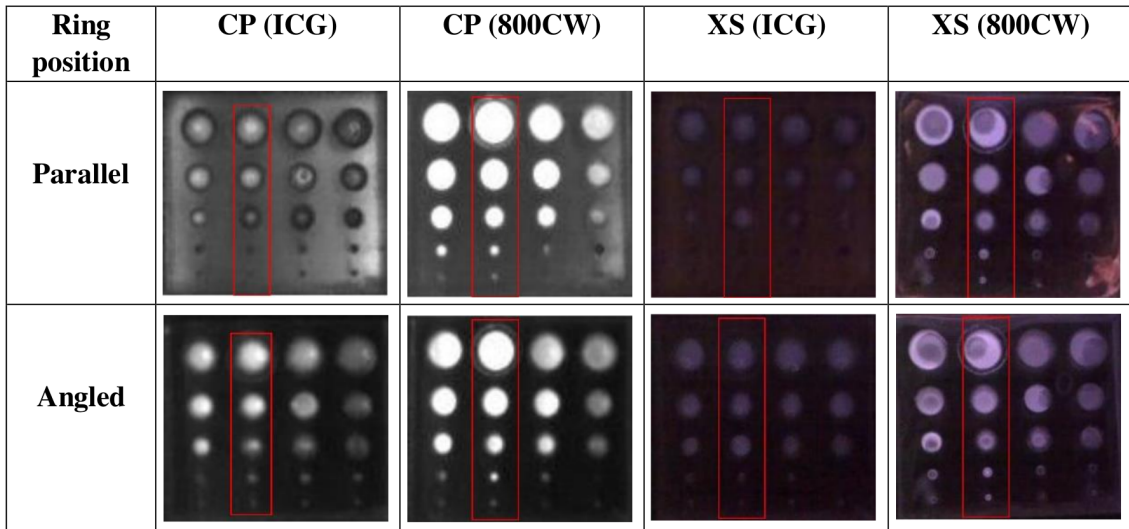| Ring position	CP (ICG)	CP (800CW)	XS (ICG)	XS (800CW)
Parallel				
Angled				

Figure 6. Example images of the MLs phantom filled with different concentrations of ICG and 800CW using CP and XS cameras at a 10 cm distance using different light source positions. The red rectangle indicates the column of different diameter wells filled with concentrations of 10 and 0.2 μM of ICG and 800CW dyes, respectively. The effect of the reflection on the imaged field can be seen in both LED positions. Air bubbles are shown within the well for 800CW using the XS camera.

As can be seen in figure 7, the CNR of the XS, using ICG and 800CW probes with angled and parallel positions of the LED ring, are plotted for all holes for one column. For both dyes, smaller wells (0.5, 1 mm) were more easily distinguished in the angled LED position due to lower backgrounds. This was because of the bright reflection resulting from the parallel position which prevented their accurate detection.

3.3 CNR as a function of target depth

The optical tissue-like phantom was used for sensitivity analysis based on depth, which was performed for both cameras using both LED ring positions. Both types of phantom, MLs and LL, were filled with fluorescence dye and imaged using both LED positions. Figure 8 shows example images of the MLs phantom filled with 800CW and imaged under different layers of the tissue-like phantom at a fixed distance (5 cm). Both NIR fluorescence cameras at both LED positions were capable of detecting smaller wells (diameters of 1 and 0.5 mm) at depths of up to 2 mm. Deterioration of spatial resolution for small wells occurred at depths greater than 3 mm due to the increased scattering effect as thickness increased. At thicknesses greater than 3 mm it became difficult to precisely detect fluorescence targets for any diameter or concentration.

Images were also taken with the LL phantom using optimal intensity concentrations of 10 μM and 0.2 μM for ICG and 800CW, respectively. An example of the images acquired is shown in figures 9 and 10 for the LL phantom filled with 800CW and placed at a 5 cm distance. It was imaged with the CP camera under thicknesses between 1 to 8 mm of scattering equivalent medium and the LED ring was placed in the parallel and the angled position. It was observed that the spatial resolution degraded at 5 mm and the fluorescence target disappeared completely at an 8 mm depth due to the increased scattering and absorption effects of the optical tissue-like phantom.
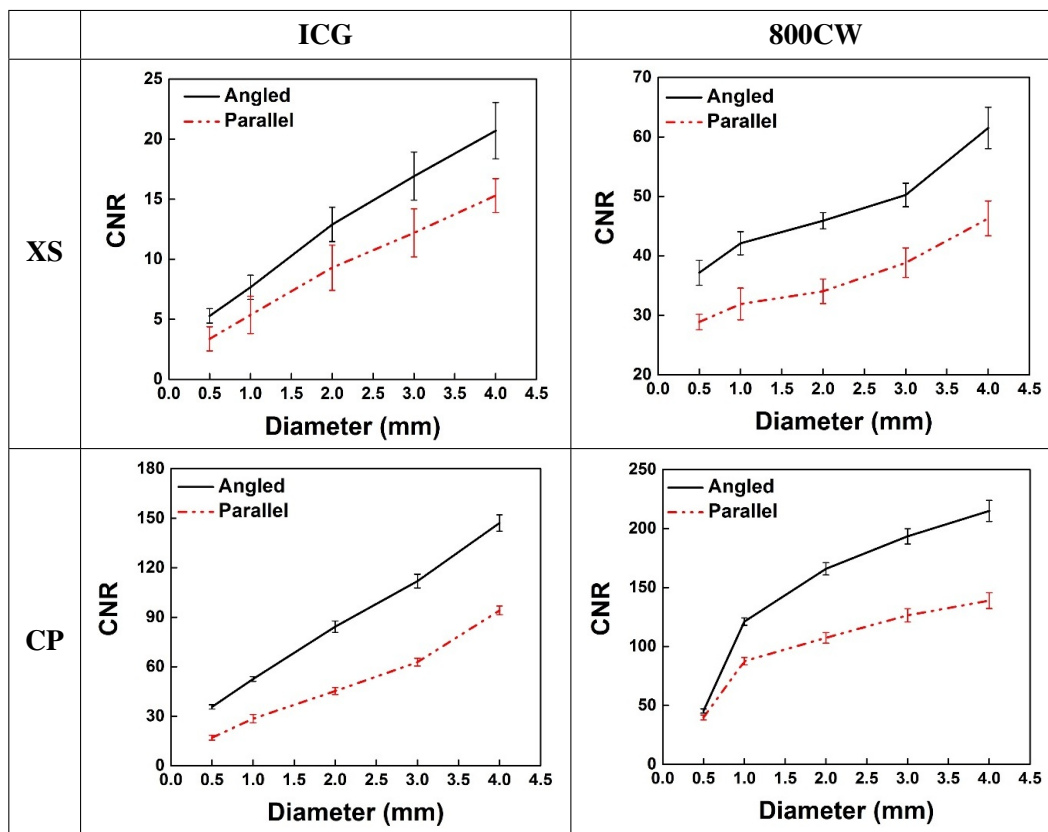
Figure 7. CNRs as a function of well diameter for the XS and CP with the ICG and 800CW. The angled position of the LED ring showed a better CNR in all setups.
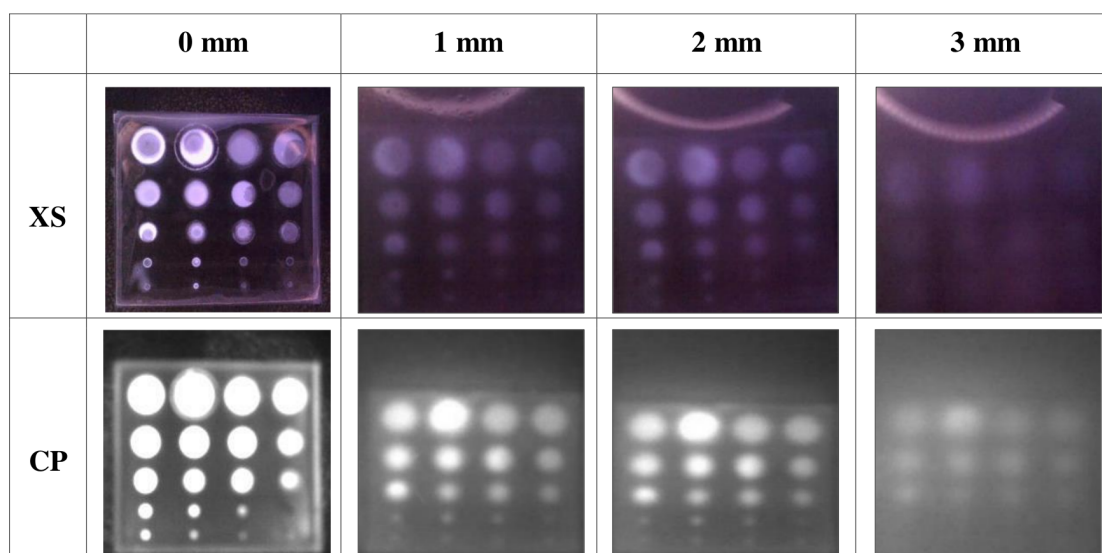

Figure 8. Example of the MLs phantom filled with different concentrations of 800CW and covered with the optical tissue-like phantom with thicknesses between 0 mm to 3 mm and imaged using the XS and CP cameras at a 5 cm distance with the LED in the angled position. 800CW can be detected up to a depth of 2 mm for the smallest hole (0.5 mm).
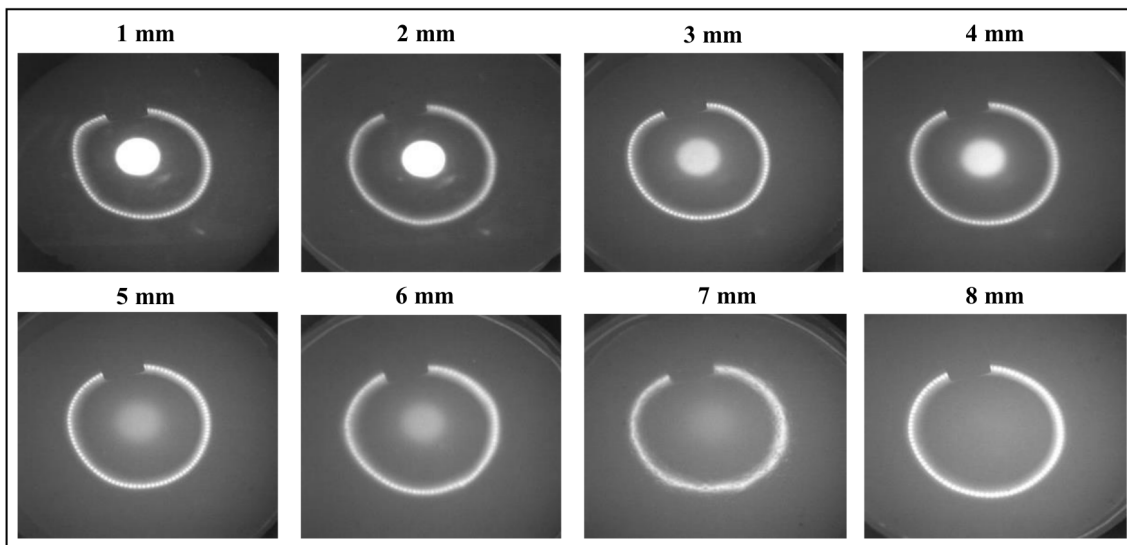
Figure 9. Images of the LL phantom containing a concentration of 0.2 μM 800CW and imaged by the CP camera. The tissue-like phantom was used with a 1 mm thickness increment. The circular ring around the fluorescence target is the reflection of the LED ring placed in the parallel.
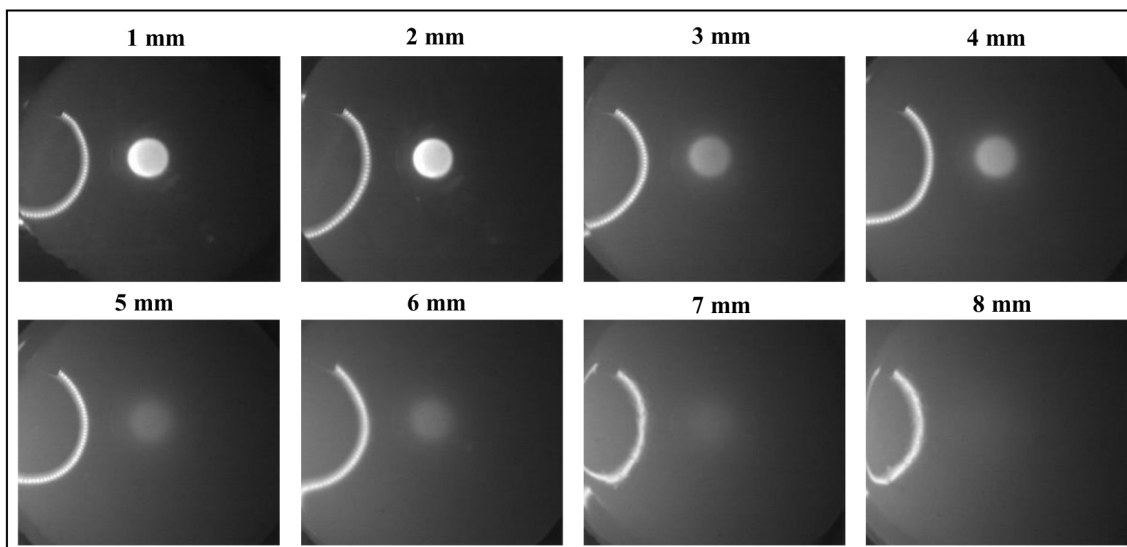

Figure 10. CP camera images of the LL phantom containing a concentration of 0.2 μM 800CW. The reflection of the circular LED ring is shown in the angular position aside from the fluorescence target.

Figure 11 illustrates CNRs for the XS and CP cameras as a function of depth using both fluorescence dyes. CNRs decrease as depth increases, until the point where the circular shape of the fluorescence target disappeared completely at 6 and 7 mm for the XS and CP, respectively.
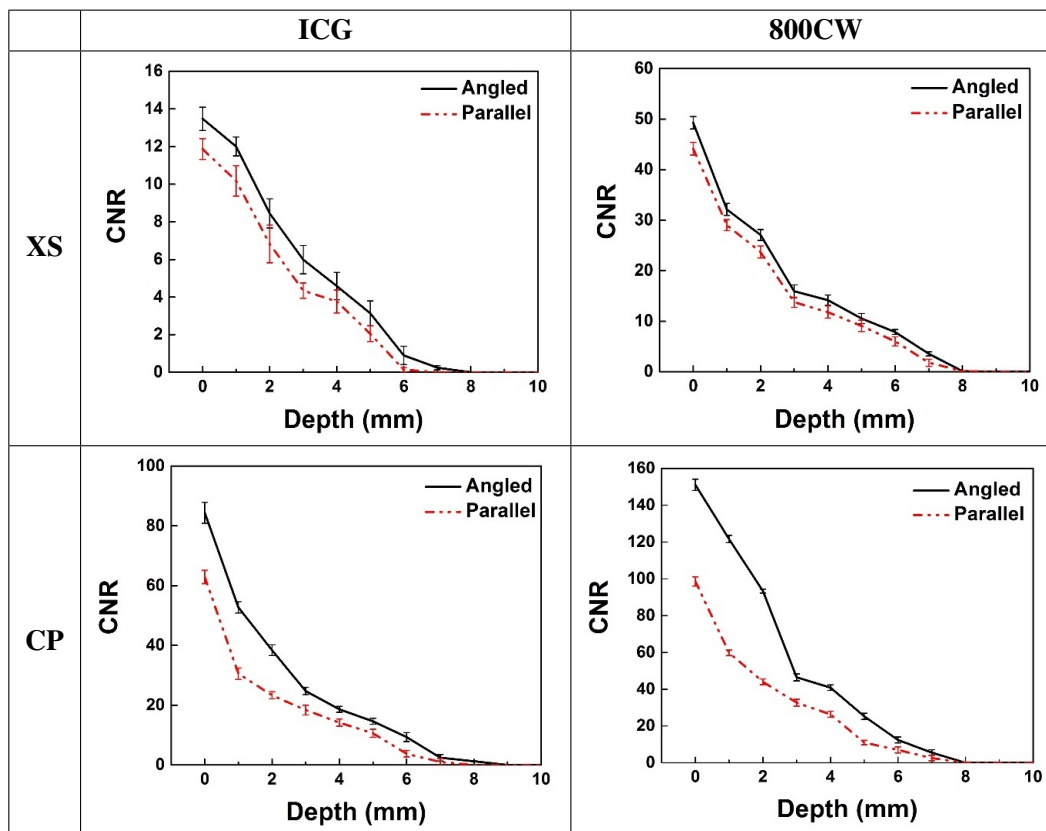
	ICG	800CW
XS		
CP		

Figure 11. CNRs as a function of thickness for the XS and CP with ICG and 800CW using the LL phantom. The angled position shows better CNRs for all cameras when using either dye. For all setups, the maximum depth that either camera could image was 7 mm.

4 Discussion

Fluorescence-guided surgery has the potential to be used in real-time imaging to assist surgeons with anatomical and functional feedback about tumour margins and vital structures. However, the main inadequacy of the NIR fluorescence imaging technique is its limited penetrative ability for targets located deeper than 1 centimetre under the skin. To tackle this limitation, a complementary combination of radioactivity and NIR fluorescence techniques have been used for SLN identification. These techniques were conducted using separate systems due to the current lack of a single real-time imaging system that combines gamma radiation with NIR fluorescence.

A hand-held hybrid gamma camera has been already developed for real-time imaging that can provide gamma and visible images simultaneously. The current development of this particular camera is to allow hybrid gamma-fluorescent imaging using hybrid radiotracers such as ICG-[99mTc]-nanocolloid or [99mTc]-Tilmanocept-800CW. In this study, the performances of two NIR fluorescence cameras were assessed in the detection of ICG and 800CW dyes. These performances were put into perspective by comparison with the Pearl and Artemis NIR fluorescence imaging systems. Moreover, the detection capabilities of both imaging systems were determined for imaging metastatic targets with various concentrations at various distances. An optical tissue-like phantom was also used in this evaluation to determine the maximum depth at which NIR fluorescence targets could be distinguished.

The efficiency of each camera, the XS and CP, was evaluated by imaging serial dilutions of ICG and 800CW. The CP camera showed a lower SNR compared to the Pearl and Artemis, while the XS exhibited the lowest SNR and CNR values using both dyes. It is worth mentioning that the XS camera is designed to provide optical and coloured images, while the other three systems are specifically manufactured for NIR fluorescence applications. The minimum and maximum detectable concentrations were extrapolated for both dyes from SNR curves of the serial dilutions. Both cameras were able to detect ICG concentrations between about 0.8 to 80 µM, while the concentration ranges for 800CW began to be observed at 10^{-2} µM and plateaued at high concentrations up to 10 µM. The optimal concentration of ICG (80 µM) was still comparable to the *in vivo* injected dose (100 µM) that has previously been used in Artemis-based studies. At low concentrations, the reflection of the excitation light had a negative influence on the sensitivity of both cameras. A diffuser plate was tested to eliminate the reflection of the LED ring on the sample, however this strongly decreased the intensity of the illumination and for this reason was not used further. The effect of the reflected excitation light on detection ability has been reported as a major challenge that limits the reduction of the noise floor when attempting to collect weaker fluorescence signals [15, 40–42].

Moreover, the metastatic phantom was used to investigate the abilities of both cameras to detect micro-volumes. The effect of the positioning of the excitation light was also investigated using both dyes. When the excitation ring was in the angled position, higher CNR values were observed, such that smaller wells (0.5, 1 mm) could be identified with a lower surrounding background signal. However, when the parallel position was used, the smaller wells could not be distinguished from the background. This was due to the fact that the photons exciting the fluorescence dyes followed a similar, contorted path as the light emitted towards the detector [10, 43]. Thus, the high amount of scattering from the excitation light at the surface of the ML phantom produced stronger light signals than the small-sized targets. This accumulation of consecutive scattering events led to random changes in the emitted photon paths and consequently prevented the accurate localisation of small-sized sources.

One of the main limitations of the fluorescence imaging technique is the limited penetrative ability due to absorption and scattering within tissues. Scattering events (i.e., changes in photon direction) occur much more frequently than absorption events [43]. Thus, to evaluate the performance of each camera, measurements using phantoms were conducted. Both cameras tested were capable of detecting ICG and 800CW as deep as 7 mm. The angled position of the excitation light also enhanced the intensity for both cameras and for both dyes. A depth of 7 mm was found to be the maximum detection depth, after which it became difficult to identify NIR fluorescence targets even with diameters as large as 10 mm using either camera or either dye in either LED ring position. For targets with smaller diameters (between 0.5–4 mm) the maximum depth for fluorescence imaging was approximately 3 mm due to the weak signal emitted from the micro-volumes used.

In general, the CP camera showed better detection abilities than the XS camera in all tests when using different dyes and LED positions. Unlike the CP, the XS camera is mainly designed for optical applications, but with appropriate modification it was able to detect NIR fluorescence targets without the need for manual adjustment of the focussing lens at each acquisition. Clearly, detection ability depends on different factors including illumination position, filtration of the excitation and emission lights, fluorophore concentration, target size and position, phantom properties and the camera system. Therefore, several improvements could be made to enhance the detection ability of the imaging system.

One possible enhancement could be focussing the excitation light to produce homogenous illumination of the target. This may allow for a reduction in the reflected light from the area of non-interest around the target by adjusting the illumination to only cover to the area being imaged. Another important improvement could be to filter the excitation light using an interference filter to block unwanted spectral ranges. Thus, further improvements are required for the NIR fluorescence imaging system, taking into account cost-effectiveness, camera size, simplicity, LED intensity and position. Further development will allow the NIR-fluorescence system to be combined with the HGC camera to enable dual radio-NIR fluorescence imaging. This would offer the possibility of simultaneously using the higher penetrative ability of gamma-ray sources with the higher spatial resolution of NIR-fluorescence in a single imaging system for intraoperative procedures.

5 Conclusions

NIR fluorescence image guidance for cancer surgery has the potential to aid surgeons in LN assessment, SLN identification, cancer staging and radical tumour resections with minimum damage to healthy and vital structures. Nevertheless, the main inadequacy with this technique is its limited penetrative ability with regards to biological tissue. Recently, several clinical studies have demonstrated a promising technique that combines gamma and NIR fluorescence modalities to enhance SLN detection accuracy. However, these techniques used two separated systems as there is currently no single hybrid system that allows for simultaneous intraoperative gamma/NIR imaging.

A hybrid gamma camera that combines gamma and optical imaging has been developed for clinical and surgical use. Further development of this system will merge the NIR fluorescence modality to provide simultaneous fluorescence-gamma imaging. In this study, NIR-fluorescence imaging systems were assessed by testing two cameras (XS and CP), two fluorescence dyes (ICG and 800CW) and different phantoms with different LED excitation positions. The minimum and maximum detectable concentrations of ICG and 800CW were determined. Moreover, the detection capabilities of both imaging systems were determined for the purpose of imaging metastatic targets using different dye concentrations. A tissue-like phantom was also used in this evaluation to determine the maximum depth at which NIR fluorescence targets could be distinguished. Further development will combine the NIR-fluorescence system with the HGC camera to enable dual radio-NIR fluorescent imaging.

---

[1]https://www2.le.ac.uk/uol/departments/iii/.

References

[1] N. Howlader et al., *SEER Cancer Statistics Review, 1975-2004*, National Cancer Institute, National Institutes of Health Bethesda, MD (2017).

[2] X.-Y. Liu, S. Pestka and Y.-F. Shi, *Preface*, in *Recent Advances in Cancer Research and Therapy*, Elsevier, Oxford (2012) [DOI:10.1016/B978-0-12-397833-2.00025-X].

[3] F.D. Dip, T. Ishizawa, N. Kokudo and R. Rosenthal, *Fluorescence Imaging for Surgeons; Concepts and Applications*, Springer International Publishing Switzerland, (2015).

[4] A.L. Vahrmeijer, M. Hutteman, J.R. van der Vorst, C.J.H. van de Velde and J.V. Frangioni, *Image-guided cancer surgery using near-infrared fluorescence*, *Nat. Rev. Clin. Oncol.* **10** (2013) 507.

[5] J.T. Alander et al., *A Review of Indocyanine Green Fluorescent Imaging in Surgery*, Int. J. Biomed. Imaging **2012** (2012) 940585.

[6] B. Ballardini et al., *The indocyanine green method is equivalent to the* ^{99m}Tc*-labeled radiotracer method for identifying the sentinel node in breast cancer: A concordance and validation study*, *Eur. J. Surg. Oncol.* **39** (2013) 1332.

[7] D. Murawa, C. Hirche, S. Dresel and M. Hünerbein, *Sentinel lymph node biopsy in breast cancer guided by indocyanine green fluorescence*, *Br. J. Surg.* **96** (2009) 1289.

[8] T. Hojo, T. Nagao, M. Kikuyama, S. Akashi and T. Kinoshita, *Evaluation of sentinel node biopsy by combined fluorescent and dye method and lymph flow for breast cancer*, *Breast* **19** (2010) 210.

[9] R. Alford et al., *Toxicity of Organic Fluorophores Used in Molecular Imaging: Literature Review*, *Mol. Imag.* **8** (2009) 7290.2009.00031.

[10] S. Gioux, H.S. Choi and J.V. Frangioni, *Image-guided surgery using invisible near-infrared light: fundamentals of clinical translation*, *Mol. Imag.* **9** (2010) 7290.2010.00034.

[11] Hamamatsu, PDE Near Infrared Fluorescence Imager, https://www.hamamatsu.com/resources/pdf/sys/SMES0026E_PDE_f_usa.pdf (2019).

[12] G.C. Gurtner et al., *Intraoperative laser angiography using the SPY system: review of the literature and recommendations for use*, *Ann. Surg. Innov. Res.* **7** (2013) 1.

[13] B.T. Lee et al., *The FLARE intraoperative near-infrared fluorescence imaging system: a first-in-human clinical trial in perforator flap breast reconstruction*, *Plast. Reconstr. Surg.* **126** (2010) 1472.

[14] Fluoptics, Fluobeam, https://fluoptics.com/en/fluobeam-us/ (2019).

[15] P.B.A.A. van Driel et al., *Characterization and Evaluation of the Artemis Camera for Fluorescence-Guided Cancer Surgery*, *Mol. Imaging Biol.* **17** (2015) 413.

[16] Biosciences, Pearl Small Animal Imagers for in vivo Optical Imaging Studies, Licor (2018).

[17] K. Polom, D. Murawa and W. Polom, *Re: Henk G. van der Poel, Tessa Buckle, Oscar R. Brouwer, Renato A. Valdés Olmos, Fijs W.B. van Leeuwen. Intraoperative Laparoscopic Fluorescence Guidance to the Sentinel Lymph Node in Prostate Cancer Patients: Clinical Proof of Concept of an Integrated Functional Imaging Approach Using a Multimodal Tracer. Eur Urol 2011;60:826–33*, *Eur. Urol.* **61** (2011) e18.

[18] O.R. Brouwer et al., *Feasibility of Sentinel Node Biopsy in Head and Neck Melanoma Using a Hybrid Radioactive and Fluorescent Tracer*, *Ann. Surg. Oncol.* **19** (2012) 1988.

[19] N.S. van den Berg et al., *Concomitant radio- and fluorescence-guided sentinel lymph node biopsy in squamous cell carcinoma of the oral cavity using ICG-(99m)Tc-nanocolloid*, *Eur. J. Nucl. Med. Mol. Imaging* **39** (2012) 1128.

[20] S. Jeschke, L. Lusuardi, A. Myatt, S. Hruby, C. Pirich and G. Janetschek, *Visualisation of the Lymph Node Pathway in Real Time by Laparoscopic Radioisotope- and Fluorescence-guided Sentinel Lymph Node Dissection in Prostate Cancer Staging*, *Urology* **80** (2012) 1080.

[21] H.G. Kang, S.H. Song, Y.B. Han, H.-Y. Lee, K.M. Kim and S.J. Hong, *Proof-of-concept of a multimodal laparoscope for simultaneous NIR/gamma/visible imaging using wavelength division multiplexing*, *Opt. Express* **26** (2018) 8325.

[22] S.L. Bugby, J.E. Lees and A.C. Perkins, *Modelling image profiles produced with a small field of view gamma camera with a single pinhole collimator*, 2012 *JINST* **7** P11025.

[23] M.S. Alqahtani, J.E. Lees, S.L. Bugby, L.K. Jambi and A.C. Perkins, *Lymphoscintigraphic imaging study for quantitative evaluation of a small field of view (SFOV) gamma camera*, 2015 *JINST* **10** P07011.

[24] S.L. Bugby, J.E. Lees, A.H. Ng, M.S. Alqahtani and A.C. Perkins, *Investigation of an SFOV hybrid gamma camera for thyroid imaging*, *Phys. Med.* **32** (2016) 290.

[25] IDS, *uEye XS USB mini camera*, https://en.ids-imaging.com/store/products/cameras/usb-2-0-cameras/ueye-xs.html (2017).

[26] IDS, *uEye CP USB camera*, https://en.ids-imaging.com/usb3-camera-ueye-cp.html?m-layered=1 (2017).

[27] S. Luo, E. Zhang, Y. Su, T. Cheng and C. Shi, *A review of NIR dyes in cancer targeting and imaging*, *Biomaterials* **32** (2011) 7127.

[28] F.A. Jolesz, *Intraoperative Imaging and Image-Guided Therapy*, Springer Science+Business Media, New York (2014).

[29] Biosciences, IRDye 800CW, https://www.licor.com/bio/products/reagents/irdye/800cw/ (2018).

[30] M.V. Marshall, D. Draney, E.M. Sevick-Muraca and D.M. Olive, *Single-Dose Intravenous Toxicity Study of IRDye 800CW in Sprague-Dawley Rats*, *Mol. Imaging Biol.* **12** (2010) 583.

[31] T. Ferreira and W. Rasband, *ImageJ User Guide*, (2012).

[32] E. Inc., LED Ring Light, Edmund Optics Inc, https://www.edmundoptics.com/ (2018).

[33] Opticalfiltershop, *Near Infrared Bandpass Filter 850nm FWHM 100nm*, https://opticalfiltershop.com/shop/bandpass-filter/near-infrared-bandpass-filter-850nm-fwhm-100nm (2018).

[34] M. Lualdi, A. Colombo, B. Farina, S. Tomatis and R. Marchesini, *A phantom with tissue-like optical properties in the visible and near infrared for use in photomedicine*, *Lasers Surg. Med.* **28** (2001) 237.

[35] PSComposites, *T-3 addition-cure silicone*, (2018).

[36] Sigma-Aldrich, *Aluminium oxide (1344-28-1)*, (2018).

[37] Max-FactorX, *Max Factor Crème Puff Deep Beige*, (2018).

[38] B. Chance, *Near-infrared images using continuous, phase-modulated, and pulsed light with quantitation of blood and blood oxygenation*, *Ann. NY Acad. Sci.* **838** (1998) 29.

[39] M. Weiler, T. Kassis and J.B. Dixon, *Sensitivity analysis of near-infrared functional lymphatic imaging*, *Proc. SPIE* **8229** (2012) 82290A.

[40] M.V. Marshall et al., *Near-Infrared Fluorescence Imaging in Humans with Indocyanine Green: A Review and Update*, *Open Surg. Oncol. J.* **2** (2010) 12.

[41] K. Hwang et al., *Improved Excitation Light Rejection Enhances Small-Animal Fluorescent Optical Imaging*, *Mol. Imag.* **4** (2005) 15353500200505142.

[42] J.P. Houston, A.B. Thompson, M. Gurfinkel and E.M. Sevick-Muraca, *Sensitivity and Depth Penetration of Continuous Wave Versus Frequency-domain Photon Migration Near-infrared Fluorescence Contrast — enhanced Imaging*, *Photochem. Photobiol.* **77** (2003) 420.

[43] S. Keereweer et al., *Optical Image-Guided Cancer Surgery: Challenges and Limitations*, *Clin. Canc. Res.* **19** (2013) 3745.